FFI RAPPORT

SYNTHETIC APERTURE SONAR SIGNAL PROCESSING: RESULTS FROM INSAS-2000

HANSEN Roy Edgar, SÆBØ Torstein Olsmo

FFI/RAPPORT-2003/02740

FFIBM/808/116

Approved
Kjeller 26. August 2003

Nils J Størkersen
Director of Research

SYNTHETIC APERTURE SONAR SIGNAL PROCESSING: RESULTS FROM INSAS-2000

HANSEN Roy Edgar, SÆBØ Torstein Olsmo

FFI/RAPPORT-2003/02740

FORSVARETS FORSKNINGSINSTITUTT
Norwegian Defence Research Establishment
P O Box 25, NO-2027 Kjeller, Norway

FORSVARETS FORSKNINGSINSTITUTT(FFI)
Norwegian Defence Research Establishment

P O BOX 25
NO-2027 KJELLER, NORWAY

UNCLASSIFIED

SECURITY CLASSIFICATION OF THIS PAGE
(when data entered)

REPORT DOCUMENTATION PAGE

1) PUBL/REPORT NUMBER	2) SECURITY CLASSIFICATION	3) NUMBER OF PAGES
FFI/RAPPORT-2003/02740	UNCLASSIFIED	34
1a) PROJECT REFERENCE	**2a) DECLASSIFICATION/DOWNGRADING SCHEDULE**	
FFIBM/808/116	-	

4) TITLE

SYNTHETIC APERTURE SONAR SIGNAL PROCESSING: RESULTS FROM INSAS-2000

5) NAMES OF AUTHOR(S) IN FULL (surname first)

HANSEN Roy Edgar, SÆBØ Torstein Olsmo

6) DISTRIBUTION STATEMENT

Approved for public release. Distribution unlimited. (Offentlig tilgjengelig)

7) INDEXING TERMS

IN ENGLISH	IN NORWEGIAN
a) Synthetic aperture sonar	a) Syntetisk aperture sonar
b) Bathymetry	b) Batymetri
c) Motion estimation	c) Bevegelsesestimering
d) Aided inertial navigation system	d) Støttet treghetsnavigasjonssystem
e) Autonomous underwater vehicle	e) Autonom undervannsfarkost

THESAURUS REFERENCE:

8) ABSTRACT

This report presents signal processing techniques particularly suited for interferometric Synthetic Aperture Sonar (SAS) systems on-board Autonomous Underwater Vehicles (AUV) (or other platforms carrying high grade navigation systems). The signal processing is applied to data collected in a controlled rail experiment at Elba Island, Italy, by SACLANTCEN, QinetiQ and FFI, using a wideband interferometric SAS and an Inertial Navigation System (INS).

We evaluate different strategies in fusing sonar micronavigation by the Displaced Phase Center Antenna (DPCA) technique with Aided INS (AINS). We obtain highest navigation accuracy using DPCA as aiding sensor into the AINS, then using raw DPCA surge and sway in combination with the AINS attitude and position.

Coarse cross correlation based bathymetry and full resolution interferometry (based on the interferogram) is tested on the full swath and objects. Coarse bathymetry is more reliable than the interferogram technique. Phase wraparounds are avoided by estimating the coarse bathymetry first, then using the full resolution phase estimates as correction. Although much work remains, this technique does show a clear potential in improving object classification ability.

9) DATE	AUTHORIZED BY	POSITION
	This page only	
26. August 2003	Nils J Størkersen	Director of Research

ISBN-82-464-0745-7

UNCLASSIFIED

SECURITY CLASSIFICATION OF THIS PAGE
(when data entered)

CONTENTS

SYNTHETIC APERTURE SONAR SIGNAL PROCESSING: RESULTS FROM INSAS-2000

1 INTRODUCTION

The Synthetic Aperture Sonar (SAS) principle is based on increasing the sonar image azimuth resolution by coherent combination of data from successive pings. The technique has the potential to improve the azimuth resolution by one order of magnitude or more compared to conventional Side Scan Sonars (SSS). SAS requires a stable slow moving platform, and SAS processing gives better results with other navigation sensors available. This makes SAS the ideal primary sensor on-board Autonomous Underwater Vehicles (AUV) performing seafloor imaging. In military applications, the SSS to SAS increase in resolution facilitates object classification at detection ranges.

This work is part of a joint project between the Norwegian Defence Research Establishment (FFI) and Kongsberg Simrad to develop a prototype interferometric SAS for the HUGIN AUV (12). The project is part of the Norwegian military AUV program (13) to deliver a prototype AUV to the Royal Norwegian Navy (RNoN) for installation on the Oksøy class mine hunters (see Fig 1.1).

FFI participates in the Joint Research Program Mine Detection and Classification at SACLANTCEN. In November 2000, a series of trials named InSAS-2000 were conducted at Elba Island (Italy) with SACLANTCEN, QinetiQ and FFI as participants (31). The basis of the experiment was to perform controlled motion of a scaled interferometric SAS on-board a trolley with a high grade Inertial Navigation System (INS). The experimental results in this report are based on the InSAS-2000 trials. Part of this report is presented at the Oceans 2003 conference (15).

Figure 1.1 The HUGIN AUV immediately before launch at the RNoN mine hunter KNM Karmøy in December 2001.

2 SYNTHETIC APERTURE SONAR SIGNAL PROCESSING

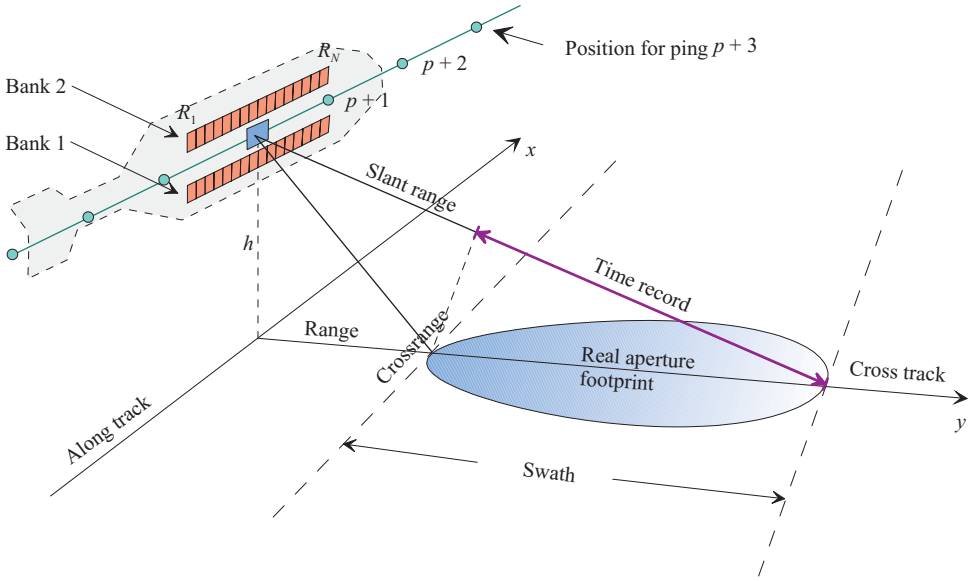

Figure 2.1 Overview of an interferometric SAS system on an AUV.

An overview of an interferometric synthetic aperture sonar mounted on an AUV is shown in Fig 2.1. The sonar consists of a phased array transmitter and two along-track receiver arrays. The length of the receiver arrays determines the area coverage rate, while the size of each element (or number of elements) determines the theoretical azimuth resolution (26), (12). Two receiver arrays are vertically displaced, giving the ability to perform interferometric processing for estimation of bathymetry. The slant-range plane is defined as the plane for which the acoustic waves are within for a given sonar location and specified range. When the AUV moves along the path, all pings are collected and stored. The data can then either be processed conventionally as a dynamically focused side scan sonar, or synthetic aperture processing can be applied.

The SAS signal processing chain shown in Fig 2.2 can be divided into four different parts:

2.1 Motion Estimation

Motion estimation, or navigation, constitutes estimation of platform motion, either from the sonar data, or an INS, or a combination of the two. Sonar micronavigation is performed by the Displaced Phase Center Antenna (DPCA) technique (25), (3), (2). The principle of DPCA is to estimate along-track displacement (surge), cross-track displacement (sway) and cross-track rotation (yaw) based on ping to ping cross correlations of overlapping transmitter-receiver pairs. This technique requires redundant sonar data by running at lower AUV speed than required by the synthetic aperture spatial sampling criterion. Hence, the coverage rate is reduced by using DPCA micronavigation. The limiting factor for DPCA alone for motion estimation is accumulated yaw error (2).

The HUGIN AUV does carry a high grade Aided Inertial Navigation System (AINS) providing attitude orders of magnitude more accurate than DPCA yaw. The theoretical accuracy of DPCA surge and sway far exceeds the accuracy of the AINS. This makes the combination of these two

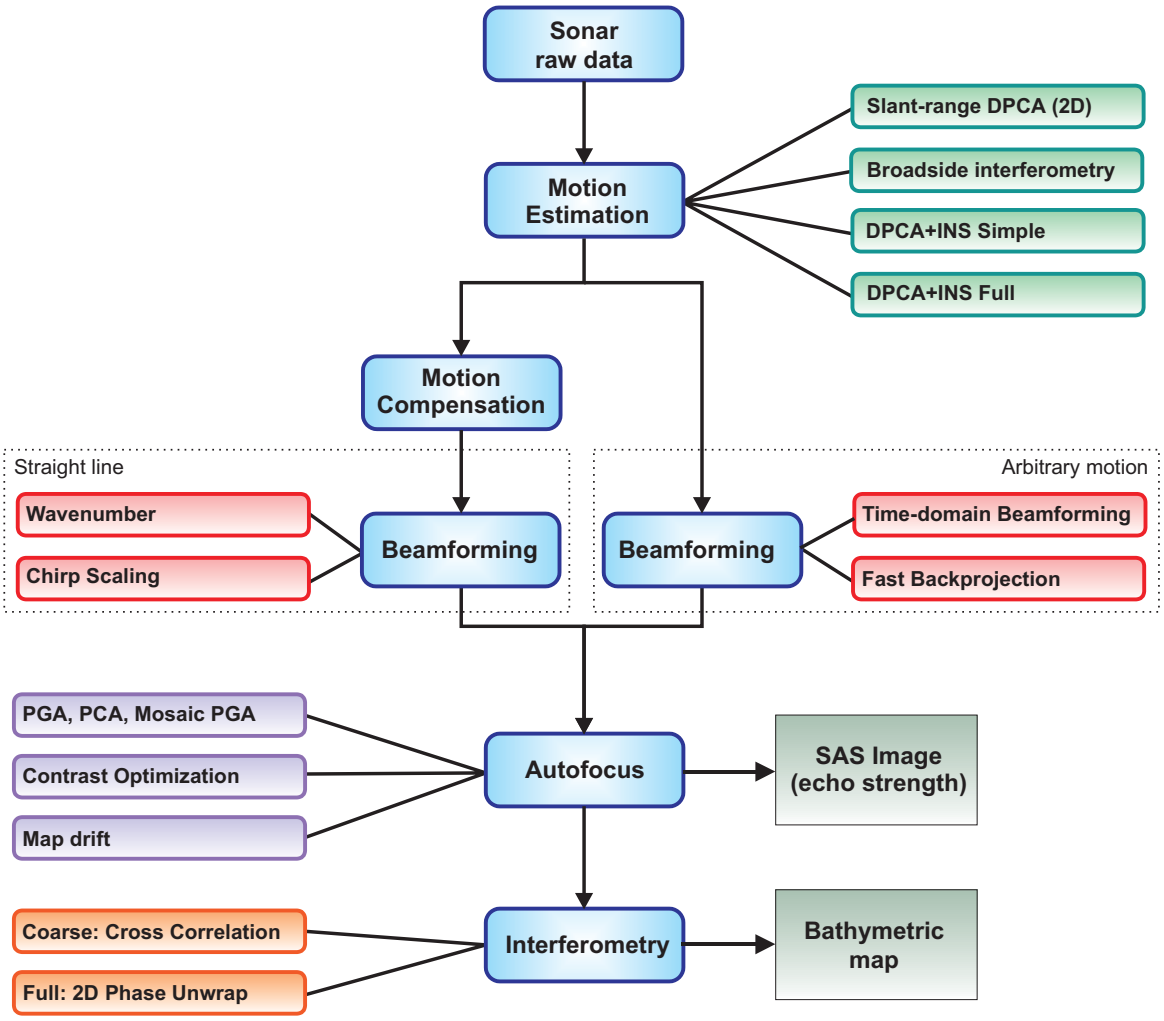

Figure 2.2 SAS Signal processing overview.

navigation techniques an attractive solution for SAS imagery (31). Fusion of DPCA micronavigation and inertial navigation also has the potential to improve the AUV navigation autonomy (19). Integrating DPCA motion estimation with INS does, however, require estimation of the depression angle in order to couple the acoustic motion estimation into the INS. Hence, swath bathymetry ping by ping (broadside interferometry) is required within the motion estimation.

2.2 Beamforming

Beamforming by synthetic aperture processing can be done in two classes of ways. Within the straight line assumption, the wavenumber (28), (17) and chirp-scaling algorithm (10) can be used. This requires, however, that motion compensation is performed before synthetic aperture imaging. These techniques are fast, but have limitations to the degree of deviation from straight line (18), (11). The other class of beamforming tolerates arbitrary motion and does not require any motion compensation. Time domain beamforming (20) is orders of magnitude slower than all other listed techniques. This is also the only technique that does not compromise any image

quality for speed. Fast factorised back-projection (30), (27) have the same computational load as the wavenumber algorithm, but on the cost of image SNR (1).

2.3 Autofocus

Autofocus are postprocessing techniques to correct for uncompensated motion errors or medium irregularities. Most of these techniques are adapted directly from the SAR community, and do not perform optimally on SAS images without modification. This is due to the fact that SAS systems are wideband and broadbeam compared to typical SAR systems (32). The Phase Gradient Algorithm (PGA) family of techniques (18), (7) show promising results in SAS autofocusing. Mapdrift autofocus is also a technique that gives clear improvement in SAS imagery (see section 4.3).

2.4 Interferometry

Interferometric processing constitutes estimation of bathymetry from vertical displaced receivers. There are two classes of techniques: Cross correlation techniques (24), (4) produce bathymetric maps at reduced resolution. Interferometry by two-dimensional phase unwrapping (10), (5) has the potential to produce full resolution bathymetric maps. Full resolution SAS interferometry with 2D phase unwrapping is non-trivial and not considered as generally solved as of today.

3 INSAS-2000 SETUP

Figure 3.1 Left: Rail. Right: Sonar with IMU and MAMA.

The sonar (right image) and the rail (left image) are shown in Fig 3.1. The sonar consists of two along-track receiver arrays and three displaced transmitters mounted on a trolley. A high grade Inertial Measurement Unit (IMU) is also placed on the trolley. A Multi Axis Motion Actuator (MAMA) was used to force different types of motion (mechanical yaw, roll and sway in addition to surge along the rail). See (31) for details regarding the experiment. Figure 3.2 shows a sidescan sonar image of the rail at the seafloor at the left side. The target field is at the lower right side outside the area with rocks, causing a slightly squinted geometry for the SAS system.

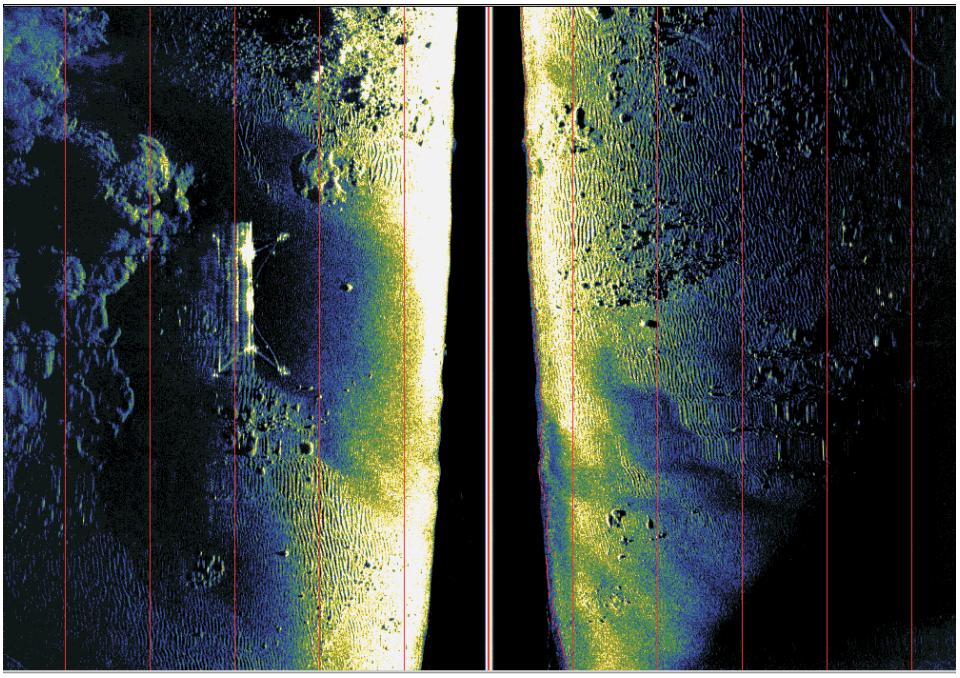

Figure 3.2 Sidescan sonar image of the rail and the footprint.

4 SYNTHETIC APERTURE IMAGE FORMATION

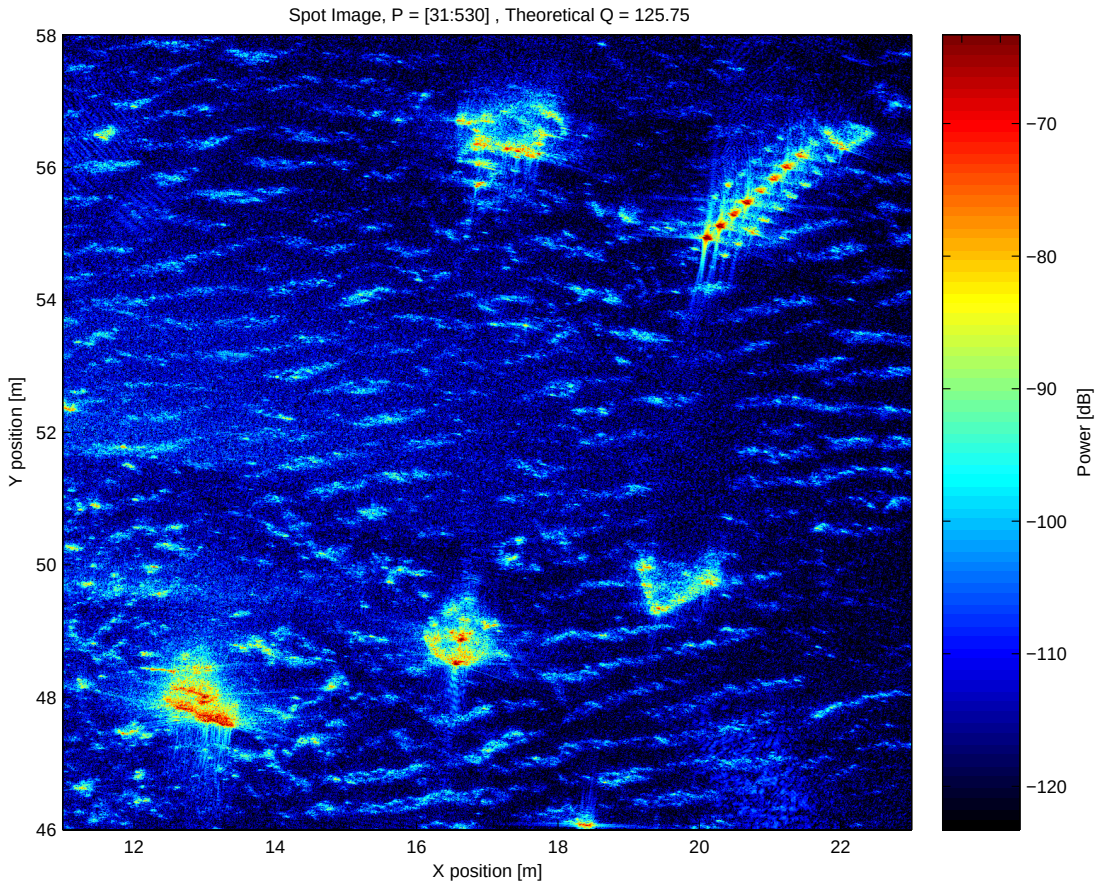

Figure 4.1 SAS image of the target field from run 221113.

Figure 4.1 shows a SAS image of run 221113 from InSAS-2000. The synthetic aperture image is produced by coherent summation of 500 pings, equivalent to 16.7 m aperture length (full length of the rail). The sonar is run with overlap factor 4 (4 times slower than required by the spatial sampling criterion for synthetic aperture imagery). This gives a theoretical SAS to sidescan sonar azimuth resolution improvement (or Q-factor) of 125.75 (2). This SAS image is produced by full integration of DPCA and INS (see the next section), dynamic focusing by time domain interpolation beamforming (20) and no autofocusing. The image contains 5 different targets: a rock placed on a turntable (lower left), a truncated cone (manta mine) (lower center), a triangular shape (rockan mine) (lower right), a bicycle (upper left) and a ladder (upper right).

In Fig 4.2 we see the SAS image from run 221107 processed in the same manner as Fig 4.1. Here the object layout is slightly different: lower left is the triangular shape on the turntable; lower center is the truncated cone; lower right is the bicycle, and upper is the ladder.

The challenge in seafloor imaging in military applications, is to produce images of such quality that man-made objects can be separated from natural objects (rocks) of equal size with highest possible precision (not missing any and not having too many false alarms). In this particular case, the two geometrical shapes on the seafloor are mine-like objects, and the stone is of similar size. Classification of objects in mine hunting is then to determine of which certainty each of the detected objects are mines.

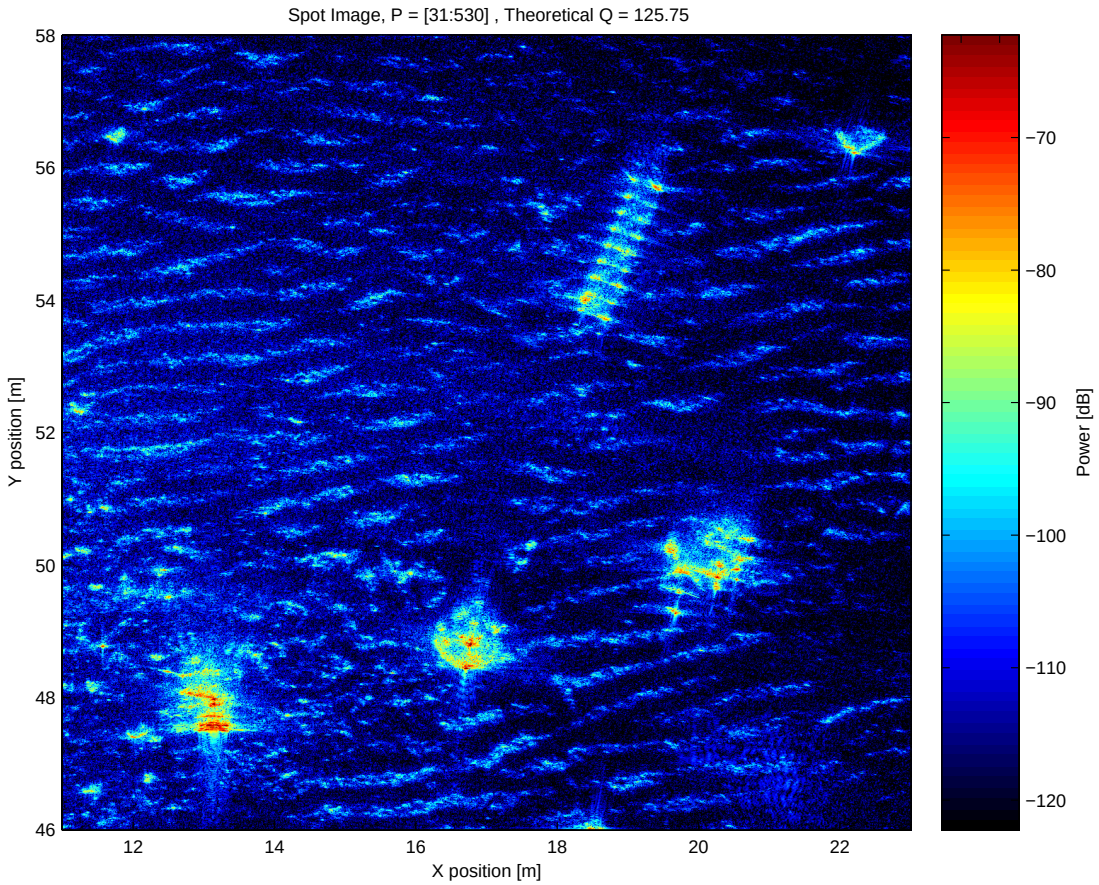

Figure 4.2 SAS image of the target field from run 221107.

4.1 Objects

Figure 4.3 shows the SAS image of the ladder from run 221113 and run 221107. The object is at different locations and with different orientation at the two runs. Both images show 8 steps on the ladder. In addition we see the start of the ladder on the center image (as a ninth step). The V-shape at the upper end of the right-most SAS image is not part of the ladder. In Fig 4.4 we see the SAS images of the bicycle from the two runs above. Again, the bicycle is relocated between the two runs, and the handlebars and pedals are in different positions. The truncated cone (manta mine) from the two runs is shown in Fig 4.5. The strongest scatterers are specular reflections from the bottom and top of the cone (shown as red dots). These are approximately 30 dB stronger than the average target strength within the object, and 50 dB stronger than the area around the object.

Figure 4.6 shows the triangular shape on the turntable from 4 different runs where the orientation of the object is changed for each run. This object is the same as the lower right in Fig 4.1 (shown in detail in Fig 4.12. The strong feature in the center of all the images does not rotate between the runs. This is actually a part of the turntable, and not a part of the object (something that misled us to mistake this for the rock on the rightmost image in (15)). The three leftmost SAS images show some resemblance of a triangular shape, although not as clear as in Fig 4.12, while the rightmost SAS image does not show any likeness. These examples show that although “superclassification” can be performed on images approaching theoretical resolution of 1.5×1.5 cm, identification of objects still is best performed with optical sensors.

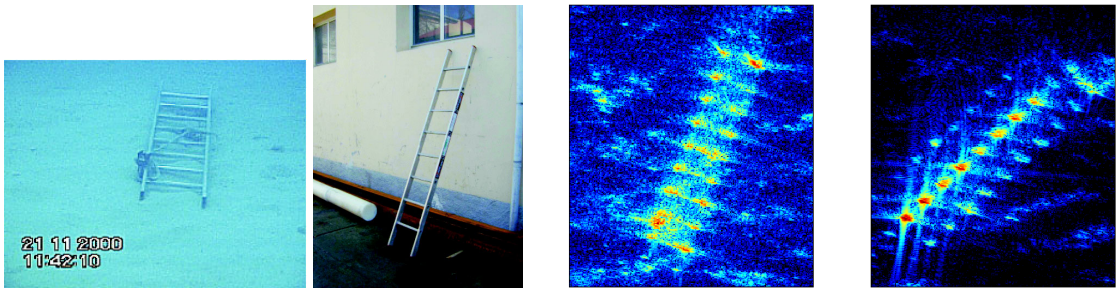

Figure 4.3 Optical images at seafloor and in air (left two) and SAS images from run 221107 and run 221113 (right two) of a 2.1 m ladder with 8 stairs.

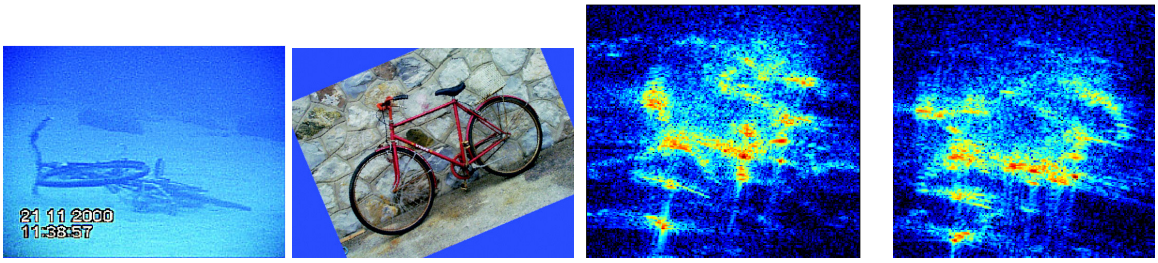

Figure 4.4 Bicycle for the same two runs as Fig 4.3.

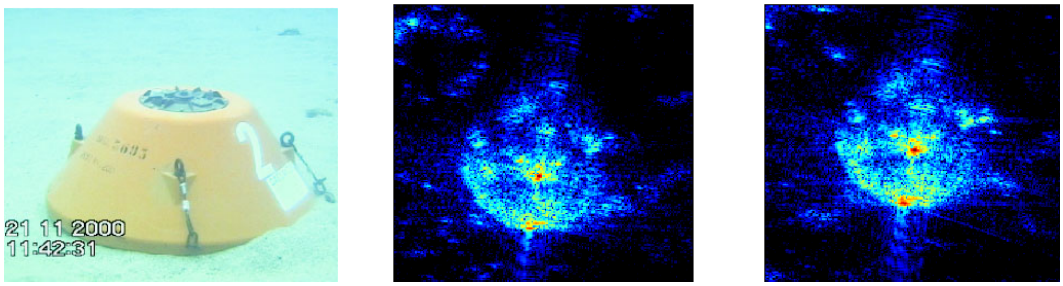

Figure 4.5 Truncated cone (manta mine) for the same two runs as Fig 4.3.

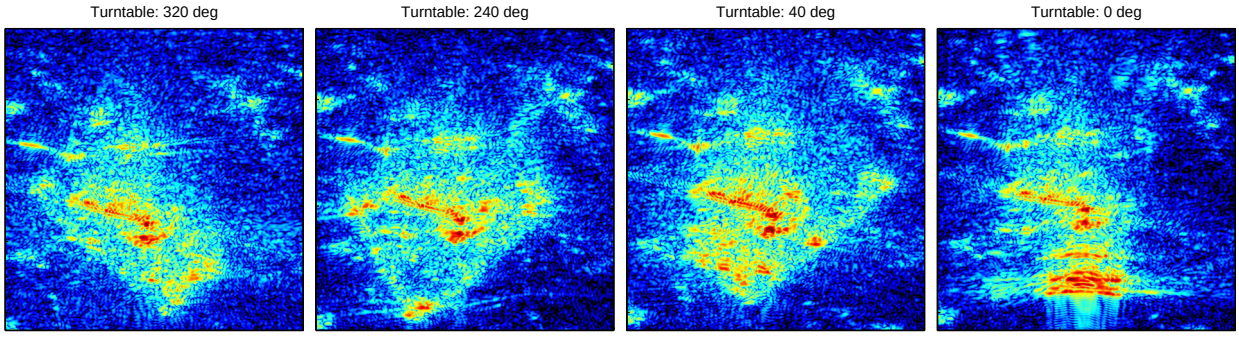

Figure 4.6 Triangular shape (rockan mine) on the turntable.

4.2 SAS vs Sidescan Sonar

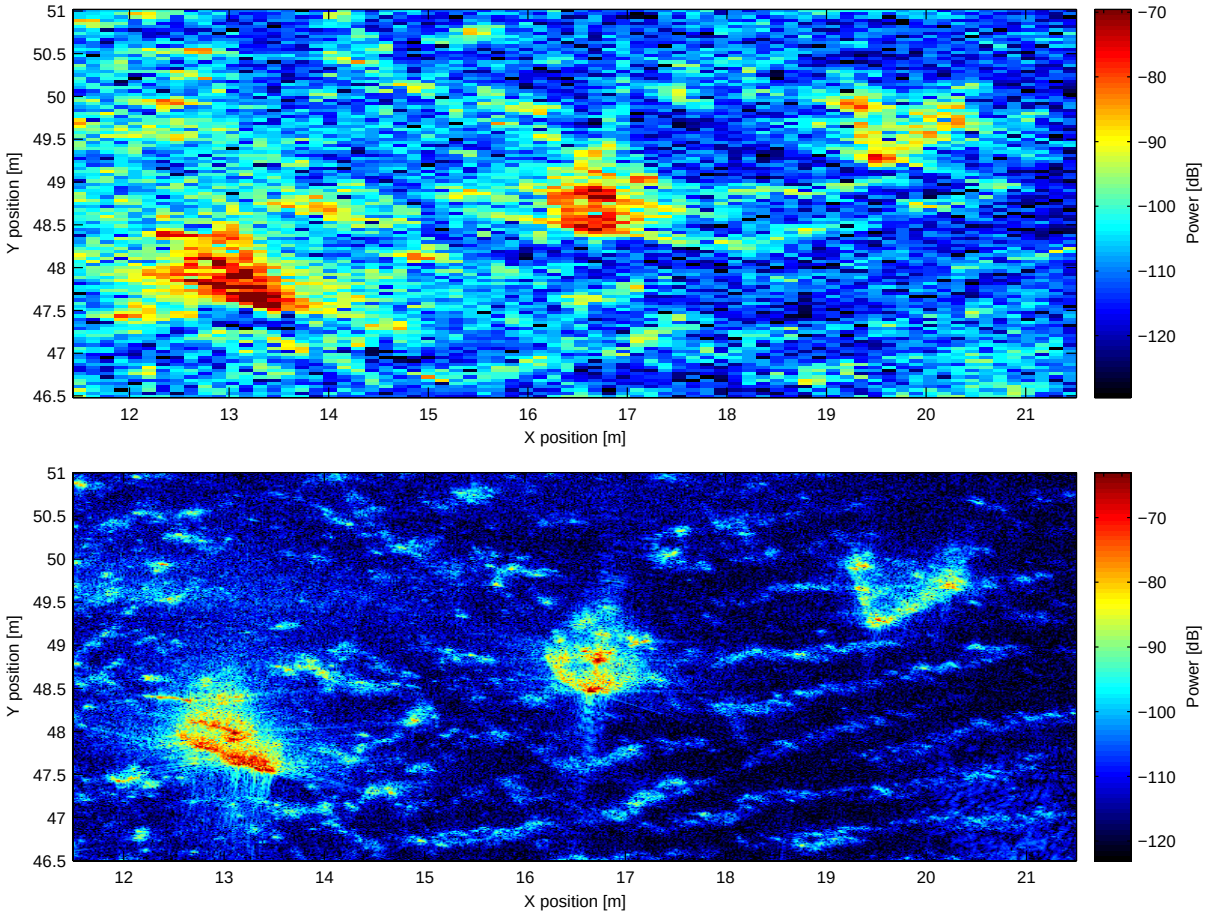

Figure 4.7 SAS image of the 3 foremost objects in Fig 4.1. Upper image: 13.7 cm azimuth resolution and 3.75 cm range resolution, equivalent to the theoretical resolution of a Klein 5400 type dynamic focused sidescan sonar at 50 m range. Lower image: 1.5 cm azimuth resolution and 1.2 cm range resolution, which is maximum resolution achieved with SAS processing.

There has been some discussion on which performance SAS processing have compared to a state-of-the-art dynamical focused sidescan sonar. Figure 4.7 shows SAS images of the 3 foremost objects in Fig 4.1. The upper image is produced with synthetic and physical resolution equivalent to a Klein 5400 SSS, while the lower image is produced with maximum resolution achieved with SAS processing at InSAS-2000.

We see that the resolution is clearly better. Image recognition is simpler. We also see that the Signal to Noise Ratio (SNR) is much higher in the lower image. This is due to the fact that in the full resolution image, 500 pings are coherently combined, while for the upper image, only 100 pings are used (equivalent to a physical array length equal to a Klein 5400).

A typical high frequency (classification type) sidescan sonar operates at around 400 kHz (the Klein 5400 operates at 455 kHz). The InSAS-2000 prototype SAS operates at 150 kHz, and the SENSOTEK SAS center frequency is at 85 kHz. The center frequency has two important implications:

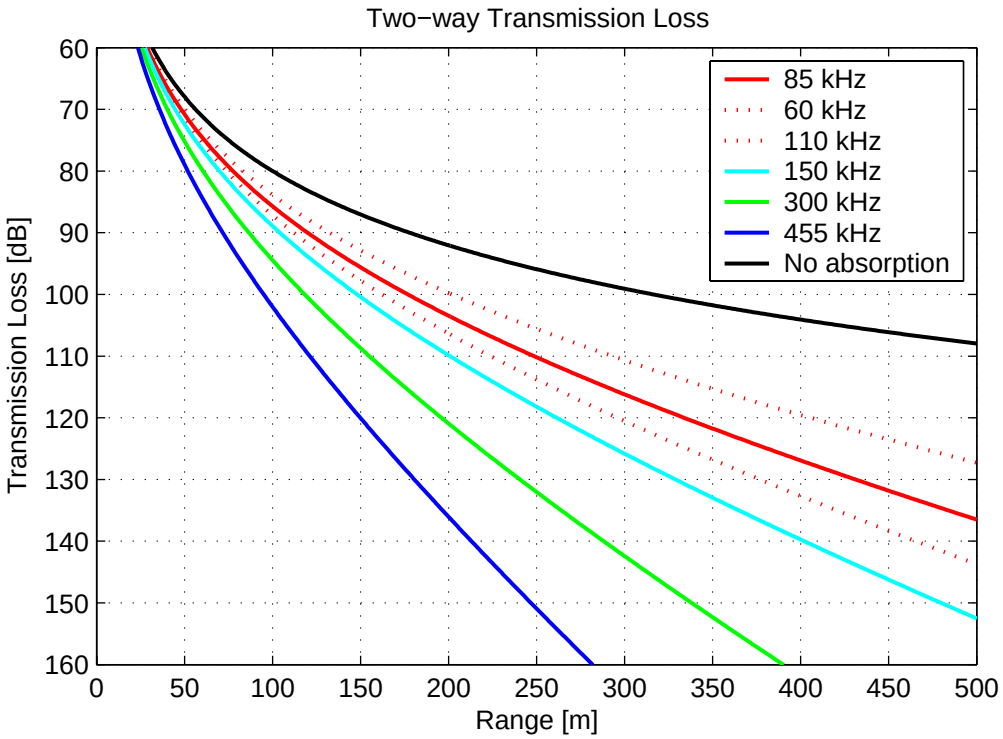

Figure 4.8 *Two-way transmission loss in the ocean at depth 100 m, temperature* 10° *C and salinity 35 ppt.*

- Sound absorption is frequency dependent. Figure 4.8 shows the two-way transmission loss in the ocean for some typical frequencies (22). If the sonar sensitivity and background noise permits a transmission loss of 110 dB, the maximum range would become 120 m at 455 kHz, 200 m at 150 kHz and 250 m at 85 kHz.
- Seafloor reflectivity is frequency dependent. Higher frequencies gives less penetrable seafloor (and objects). This could give different enhancements of features in the sonar images at 455 kHz and 150 kHz.

Figure 4.9 shows the SAS image (upper) and the sidescan image (lower) of the full scene from InSAS-2000. The sidescan image is from a hull mounted 384 kHz sidescan sonar on-board a ship surveying the area (same image as shown in Fig 3.2). Note that this comparison may be unfair to the sidescan sonar, since what we show here is a screen dump from the sidescan sonar viewing software. We do, however, see the clear effect of range dependent seafloor reflectivity and transmission loss for the sidescan sonar.

Traditional classification sidescan sonars have the highest possible frequency limited by the maximum range of the system in order to produce the highest possible azimuth resolution. SAS systems have no such limitation since the synthetic array gives the azimuth resolution. The physical array length along-track is, however, directly related to the coverage rate for SAS systems. See (14) for relation between design of SAS systems and calculation of resolution and coverage rates.

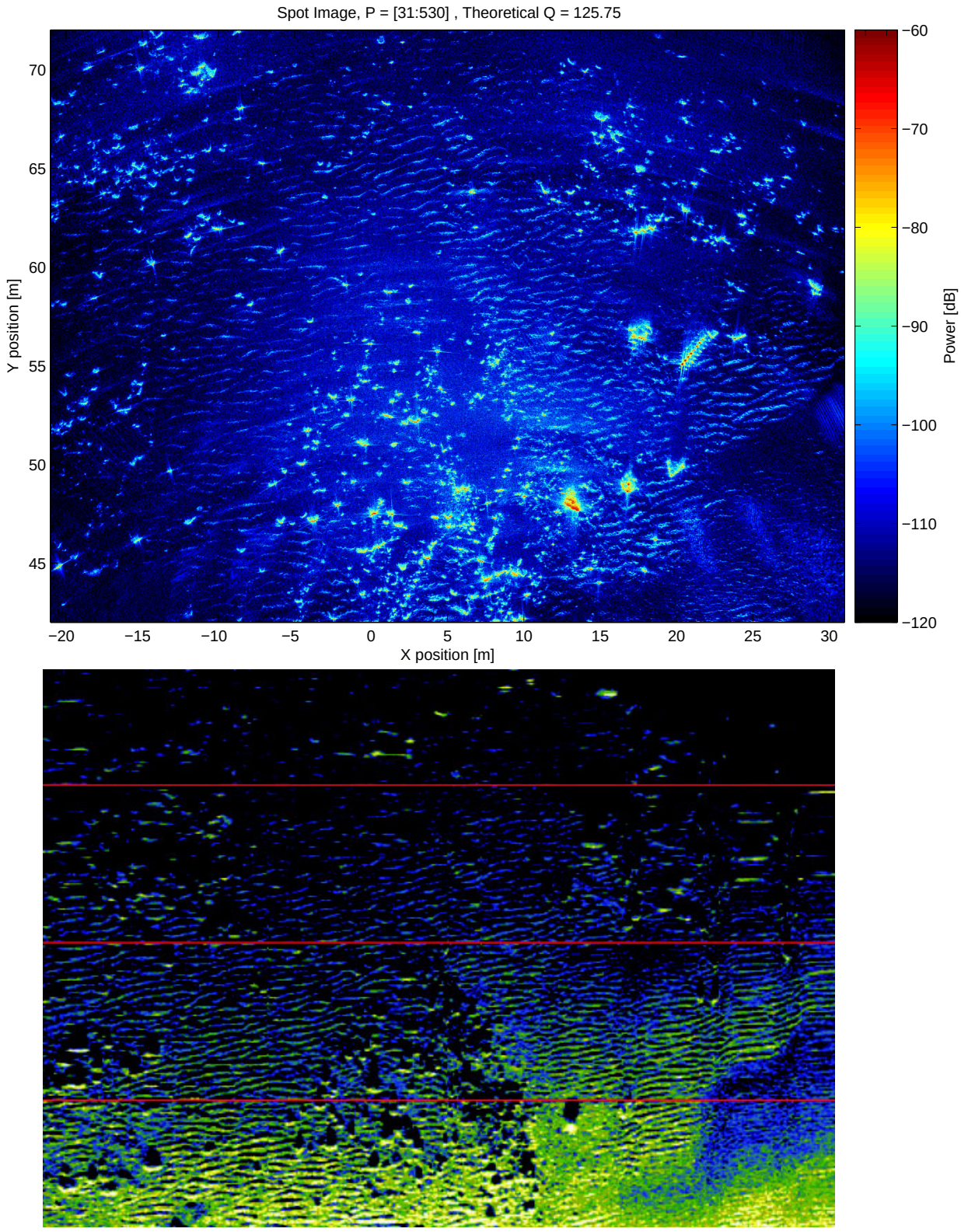

Figure 4.9 Sidescan image (lower) and SAS image (upper) of the full SAS footprint. The red lines in the sidescan image indicates 10 m marks in slant-range.

4.3 Subaperture Processing

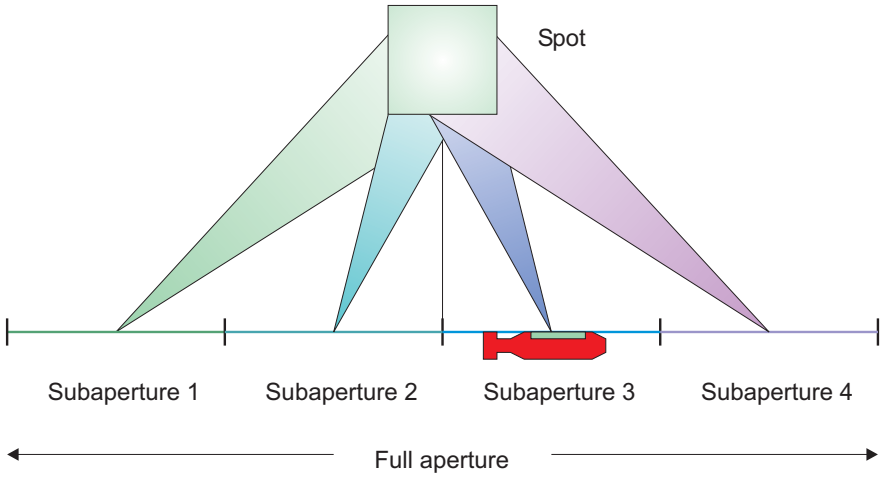

Figure 4.10 Subaperture processing overview.

Subaperture processing is dividing the full length of the synthetic aperture (determined by the azimuth beamwidth of the transducers) into subapertures as illustrated in Fig 4.10. A SAS image of the same scene is produced from each subaperture, giving independent images with lower along-track resolution. These subaperture images can be used in a number of ways for different purposes:

Multi-Aspect Classification
Multi-aspect processing promises to improve the classification capability by producing several aspects (or look directions) and thereby different highlights and shadows of the same object (8). Figure 4.11 shows SAS images generated by a subaperture based on 180 pings of the leftmost, center and rightmost part of the rail. The effect of multi-aspect processing is somewhat limited due to the short rail in this particular experiment. We see, however, that the shadow and the specular point on the left object are changed for each aspect.

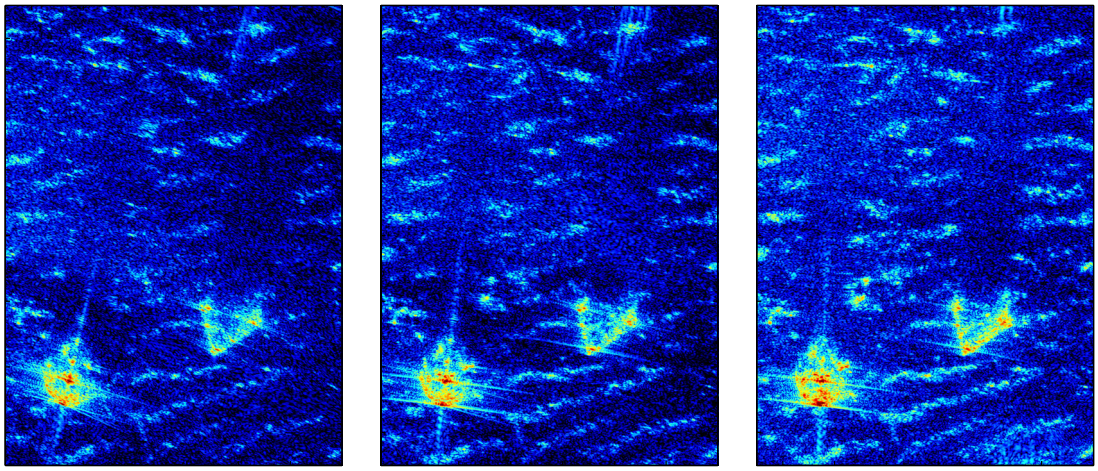

Figure 4.11 SAS images of 2 objects from Fig 4.1 based on a subaperture of 180 pings. Left: leftmost part; Center: center part; Right: rightmost part.

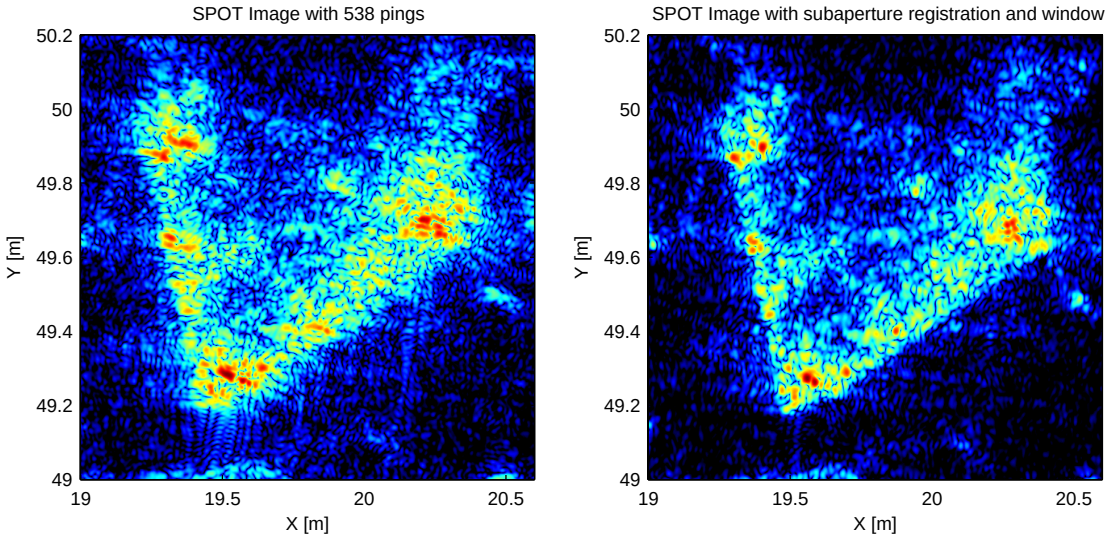

Figure 4.12 Mapdrift autofocus technique. Left: original SAS image. Right: SAS image after mapdrift autofocus based on 5 subapertures.

Multi-look processing

Multi-look processing (from the SAR community) is incoherent addition of the subaperture images in order to reduce speckle (18). Speckle is coherent summation of individual scatterers within one resolution cell and produces noise-like image characteristics of all coherent imaging systems where the physical resolution is large compared to the wavelength (23). Full aperture SAS images from InSAS-2000 have a resolution of 1.5×1.5 wavelength, and should therefore be close to speckle-free (29). Statistical analysis of the SAS images from InSAS-2000 produced at lower resolution both in range and azimuth, shows, however, little evidence of speckle (16). The reason for this is not known. Other work show some effect of speckle reduction by multi-look processing of SAS images (9).

Mapdrift Autofocus

Mapdrift autofocus is a technique where position differences between each subaperture image is estimated and used in order to correct the trajectory (6). Figure 4.12 shows the original SAS image based on the full length of the synthetic aperture (left), and the corresponding SAS image after mapdrift autofocus (right). The autofocusing is done by dividing into 5 subapertures, estimating the image displacement, and producing a polynomial correction to the cross-track position. The SAS image is then recalculated using the modified full length of the synthetic aperture.

4.4 Image Degradation

Position and orientation errors along the synthetic aperture may cause image blurring (defocus) and grating lobes. These types of errors only appear in SAS images and do not exist in sidescan sonar images. Figure 4.13 shows a SAS image of the target field from a run with mechanical yaw. A lever arm error causes grating lobes around strong reflectors (left image). Note the ladder (upper right object) compared to Fig 4.1. By reducing the overlap factor (redundancy) in the synthetic aperture, the grating lobes and the general noise level increases (center image). The

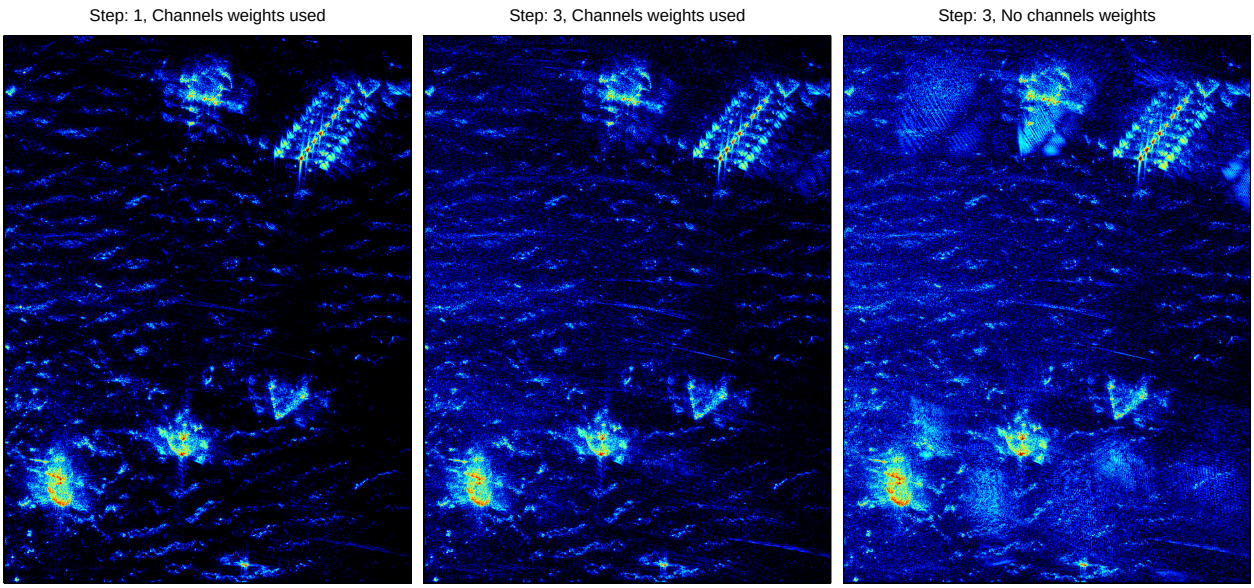

Figure 4.13 SAS image from a run with mechanical yaw and incorrect navigation (lever arm). The repetitive aperture error causes grating lobes in the image. This is worsened by reducing overlap (increasing step) and turning off the channel weighting along the aperture.

right image shows the same synthetic aperture sampling as the center image, but without channel weighting (compensation for uneven overlap along the synthetic aperture). We see that even more image artifacts appears.

The grating lobes appear as focused reflectors in the image, and can easily be mistaken for objects. Care must therefore be taken in the SAS processing, especially in the navigation, to minimize such effects.

5 SONAR NAVIGATION

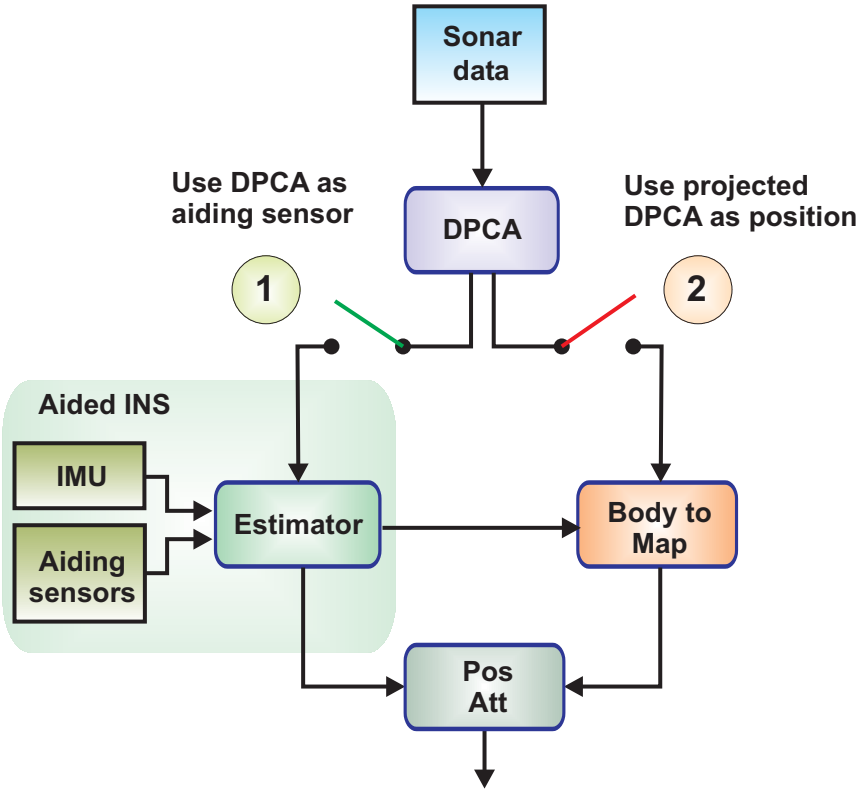

Figure 5.1 Integration of DPCA micronavigation into the Aided INS.

Accurate navigation is crucial for optimal use of synthetic aperture sonar. A maximum phase-error of $\pi/4$ along the synthetic aperture leads to a position accuracy of $\lambda/16$, equivalent to 1 mm for InSAS-2000. This accuracy is unrealistic for AUV motion along a synthetic aperture of 10 - 100 m with traditional navigation techniques.

There are usually measurements from three different sets of navigation sensors available: the IMU, DPCA and other aiding sensors such as a Doppler Velocity Logger (DVL). Figure 5.1 shows possible ways to combine these sensors. If switch 1 and 2 are both open, only IMU measurements and aiding sensors are used and evaluated in an error-state Kalman filter (INS).

DPCA can be treated as (a highly accurate) delta sensor. Closing switch number 1 adds DPCA as aiding sensor into the Kalman filter (DPCA-AINS). This integration requires the knowledge of the direction of the acoustic axis relative to the AUV (or slant-range direction, see Fig 2.1) for each ping, which can be obtained by interferometry. Alternatively, we can close switch 2 and use full integration of INS and DPCA. This technique consists of rotating the INS measurements into body coordinates, replacing the calculated surge and sway with DPCA measurements, and rotate the fused data back into map coordinates (INS & DPCA). Also this integration technique requires ping by ping slant-range direction. Finally, it is possible to use both integrations simultaneously (DPCA-AINS & DPCA). This is the method we have used in this report, unless specifically stated otherwise.

We have tested the four methods described above together with pure DPCA micronavigation and straight line assumption on run 221107 from InSAS-2000. The SAS images based on these 6

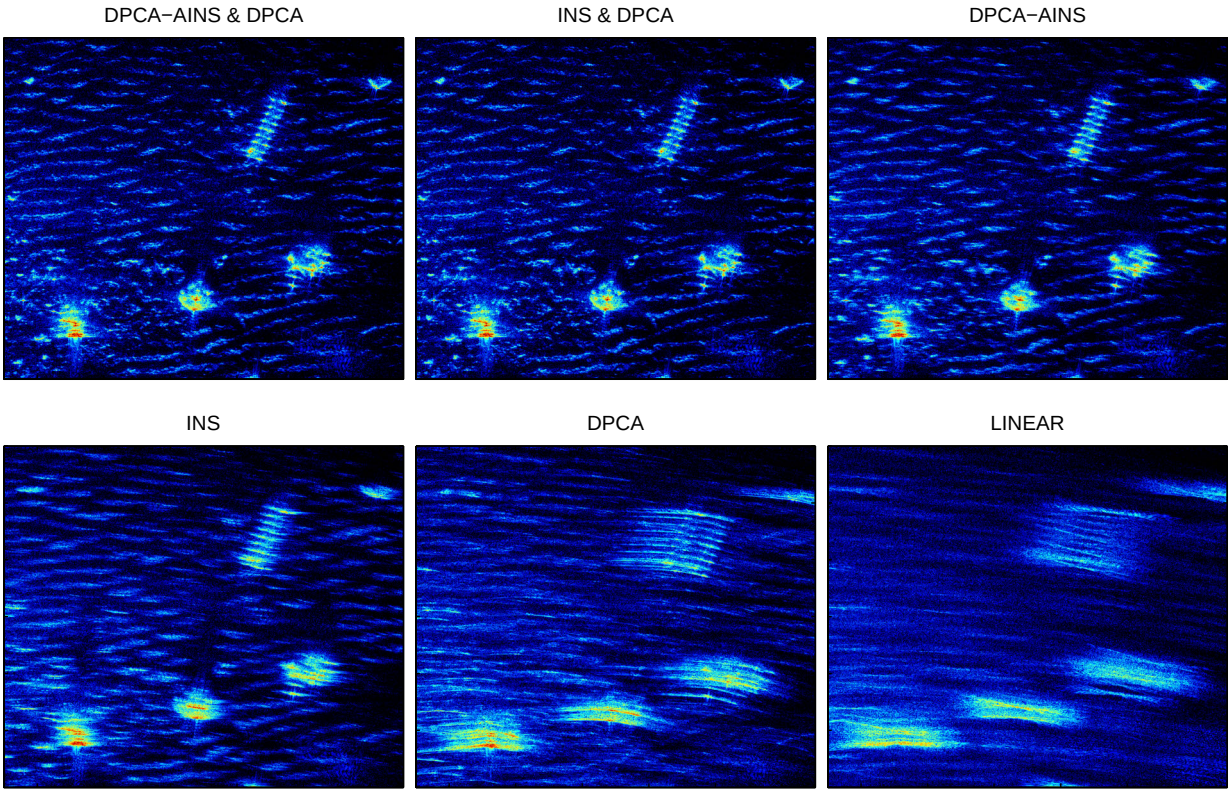

Figure 5.2 SAS Images produced by 6 different strategies of combining DPCA and INS.

navigation strategies are shown in Fig 5.2. The images are produced with resolution 1×1 cm based on 500 pings.

The visible effect of using DPCA as aiding sensor is marginal when also using full integration of DPCA and INS. Hence, DPCA surge and sway as aiding sensors have little impact on INS attitude. This is probably due to the short synthetic aperture (limited by the rail) and the short range in this particular experiment. In typical scenarios for AUV based SAS, DPCA aided INS have the potential to improve both the synthetic aperture length and the AUV navigation ability.

DPCA as aiding sensor without full integration gives slight blurring, but is substantially better than INS only. Assuming linear trajectory or using pure DPCA navigation result in clearly defocused images (as expected). Note that the synthetic aperture is approximately 6 times longer than the CRLB of DPCA micronavigation alone (31), (2). In addition, this comparison is somewhat unfair to DPCA micronavigation alone since there is a known bias in the DPCA yaw estimate due to imperfect hardware.

Figure 5.3 shows the cumulative contrast for the images in Fig 5.2. All methods except linear assumption are almost equally good after 50 pings (1.7 m synthetic aperture). After that, the contrasts diverge as expected. Theoretically, using DPCA as aiding sensor alone should have been sufficient assuming no fluctuations in the ocean. The poor performance may in addition be caused by either an incorrect lever-arm between the IMU and the sonar, or an inaccurate specification of DPCA-accuracy in the Kalman filter. Figure 5.3 also indicates that full integration of DPCA in addition to DPCA as an aiding-sensor is the optimal method for this dataset.

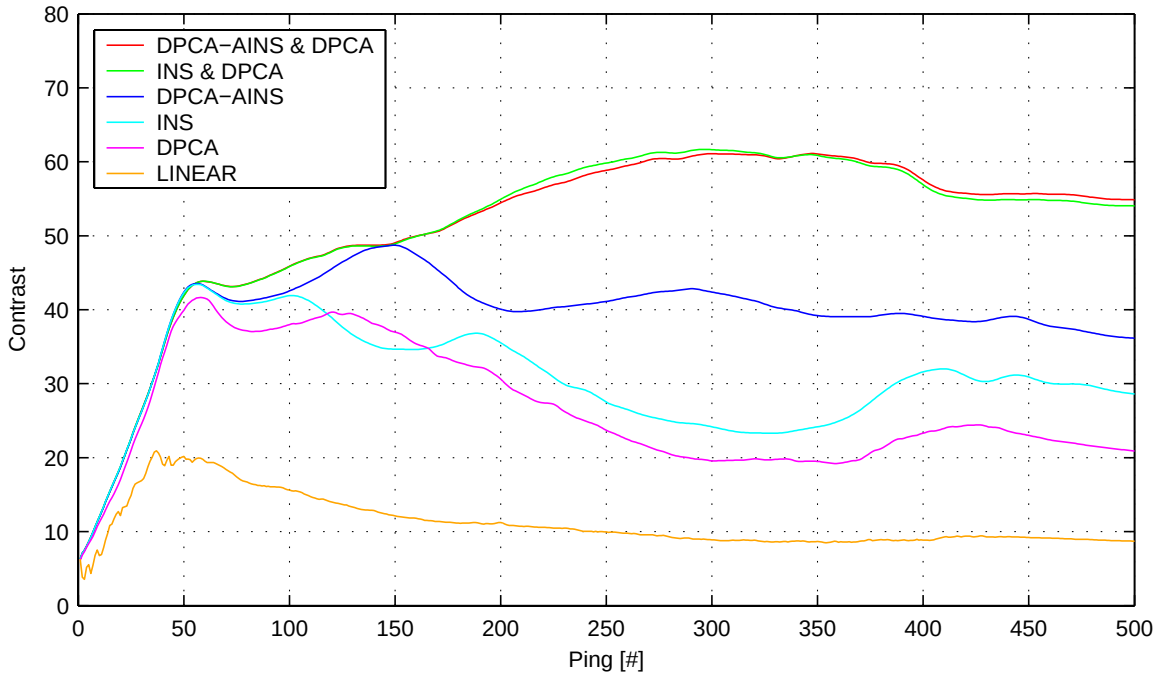

Figure 5.3 Cumulative contrast for the corresponding images shown in Fig 5.2.

6 SWATH BATHYMETRY

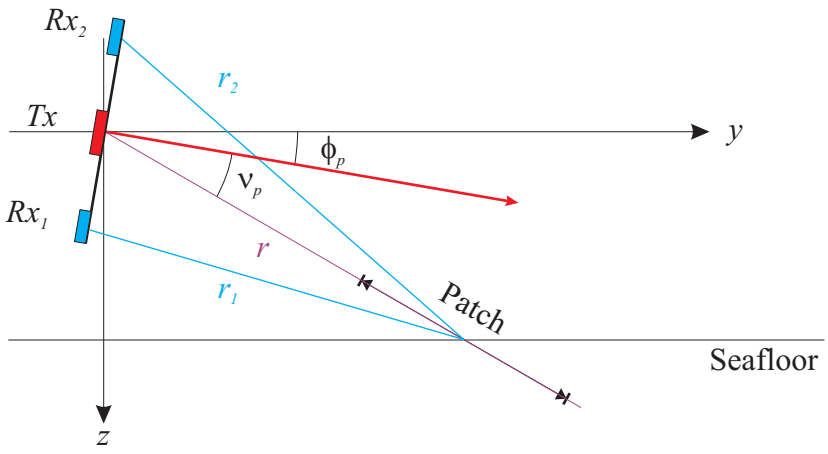

Figure 6.1 Principle of interferometric height estimation.

The basic principle of interferometry is to measure the difference in travel time between the returned echos for two separate receiver banks (21). Figure 6.1 shows a simplified interferometric geometry for a sonar with roll ϕ_{p}. The slant-range direction to the seafloor relative to the platform roll, ν_{p}, is simply

$$\nu_{\mathrm{p}} = \arcsin\left(\frac{c\tau}{B}\right), \tag{6.1}$$

where c is the sound velocity, τ the difference in travel time and B the baseline between the receiver banks. The corresponding height above the seafloor, H, is then

$$H = r\sin(\nu_{\mathrm{p}} + \phi_{\mathrm{p}}), \tag{6.2}$$

where r is the distance between the sonar and the seafloor.

Although the principle is the same, a slightly more complicated algorithm is needed when the SAS images from bank 1 and 2 are focused at a specific height.

The non-trivial part of interferometry is, however, estimating the lag accurately. We have tested two different methods. The most robust of these estimates a coarse bathymetric map, based on complex cross correlation of patches along y (24). For each of the two banks, we select a small stripe of the image along y, cross correlate them and estimate the lag. To ensure both sufficient data in the correlation and a useful resolution in the bathymetric maps, we oversample the images along y. Significant overlap is also used in the correlation windows. The resulting bathymetric maps have full resolution in x, but are lowpass filtered in y. This technique is limited by baseline decorrelation (or geometrical distortions) at near range and low Signal to Noise Ratio (SNR) at far range.

The bathymetry of the full scene in InSAS-2000 is shown in Fig 6.2. The rock can be seen at $x = 13\ \mathrm{m}, y = 48\ \mathrm{m}$. Note that the height deviation is less than 4 m on an area of approximately $1350\mathrm{m}^2$. The corresponding SAS-images where calculated with a resolution of 5×0.1 cm and focused at a flat seafloor of approximately 12.5 m. Then a correlation window of 1 m is displaced with intervals of 5 cm along each stripe. The gridding in the bathymetric map is therefore 5×5

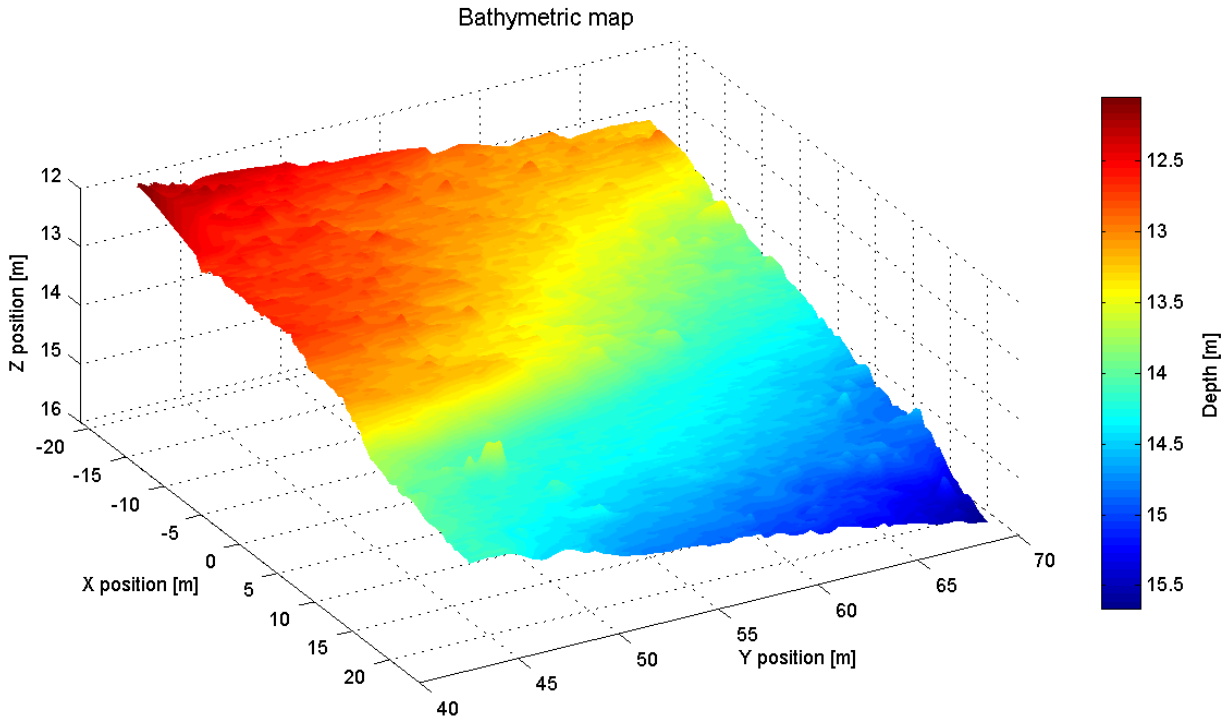

Figure 6.2 Bathymetric image of full scene of InSAS-2000.

cm. Areas with low coherence are interpolated and the resulting data is also smoothed with a block size of 5×5 pixels. Note that the interpolation fills the shadows in the SAS image with valid heights from nearby areas. This is extremely hazardous, since man-made objects (i.e. mines) within the shadow areas vanish in the bathymetric map. The proper way to handle this is to leave the shadow areas with no valid height.

Figure 6.3 shows the three foremost objects from run 221113 (see Fig 4.1). The rock (leftmost object) is, as expected, most dominant. Compared to the SAS image, there is a small displacement of the objects, which partially is caused by focusing at incorrect height. The shape of the objects are also slightly distorted. The bathymetric map in Fig 6.3 is calculated with the same parameters as the map in Fig 6.2, except that the SAS images originally had 1 cm resolution along-track. Complex averaging is used to resample the images to 5 cm and consequently the noise is reduced.

Another possible approach is to estimate the lag by computing the interferogram (10). This method has no smoothing along y and has potential to achieve the same resolution in the bathymetric map as in the SAS images. However, one of the main difficulties is the need for 2D phase unwrapping. This problem can be avoided by using coarse cross correlation based height as input to the imaging, thus avoiding phase wrapping in the interferogram. Alternatively, the coarse estimate can be used to calculate a synthetic interferogram which is subtracted from the measured interferogram. The calculated height is then a correction to the coarse estimate.

6.1 Bathymetry in Object Classification

High resolution bathymetric imagery of objects have potential to dramatically increase the classification ability, along-side other techniques such as multi-aspect classification. The two

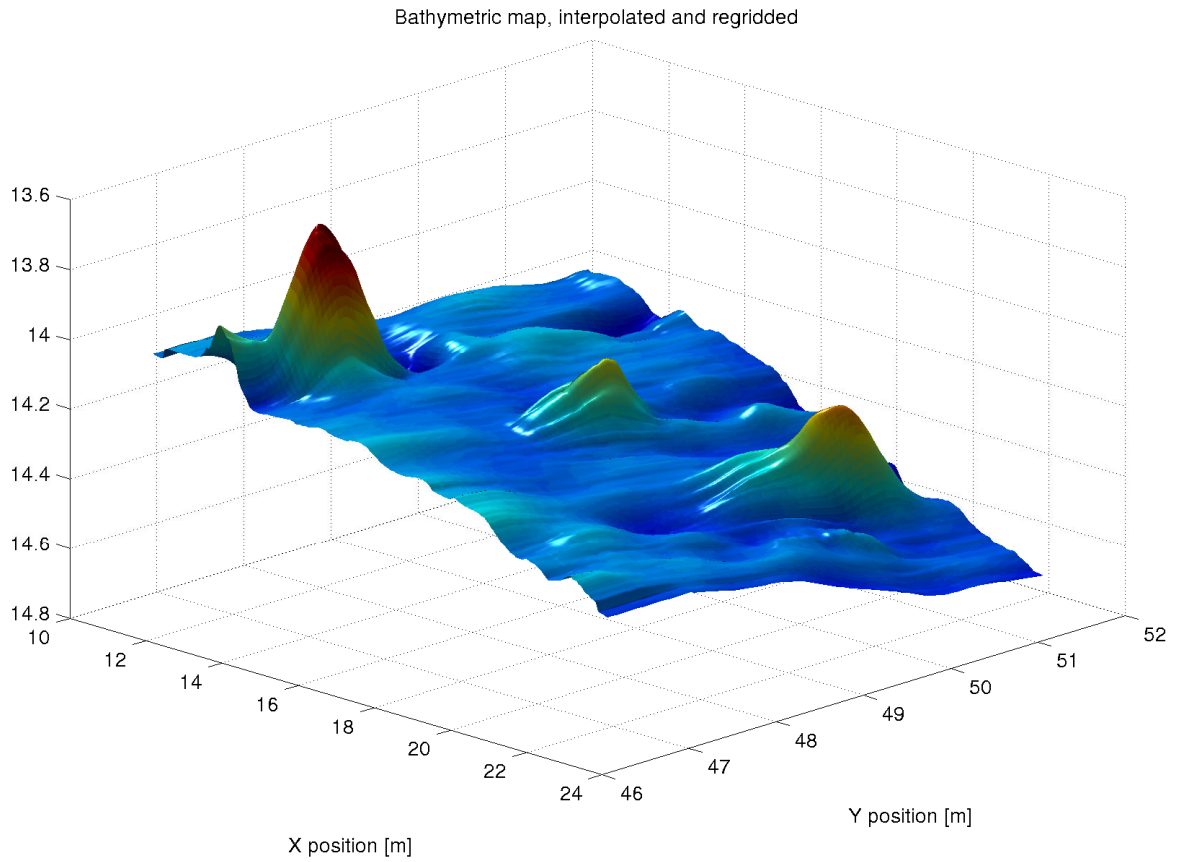

Figure 6.3 Bathymetric image of the three foremost objects in run 221113 (see Fig 4.1).

techniques outlined above is applied to a high resolution image of the rock on the turntable from run 221113. Figure 6.4 shows an optical image (upper left), the SAS image (upper right), coarse bathymetry (lower left) and full-resolution bathymetry (lower right). The synthetic resolution in the SAS images is originally 1×1 mm, then resampled to 5×0.1 cm in the coarse bathymetry and 5×5 cm in the full resolution method.

The orientation of the rock is visible with both methods, but some additional aspects may be worth commenting: The full resolution bathymetry seems equally smooth as the coarse estimate and also more inaccurate. This is caused by a high noise level in the interferogram. To achieve useful results, we apply median filters, remove bad data and apply smoothing. Therefore, the final map is comparable to the coarse estimate in resolution. The main features are, however, clearly visible in both figures. The rock is oriented along x with the highest point toward negative x. Note also that the feature in the center of the SAS image is not a part of the rock. It is actually a part of the turntable. This is easily seen in Fig 4.6, where another object is placed on the turntable and rotated.

A major limitation to both techniques of bathymetric processing is grating lobes caused by imperfect navigation, and sidelobes. Both effects reduce the ability to properly map areas around strong reflectors, something that is essential for proper 3D object shaping with bathymetry.

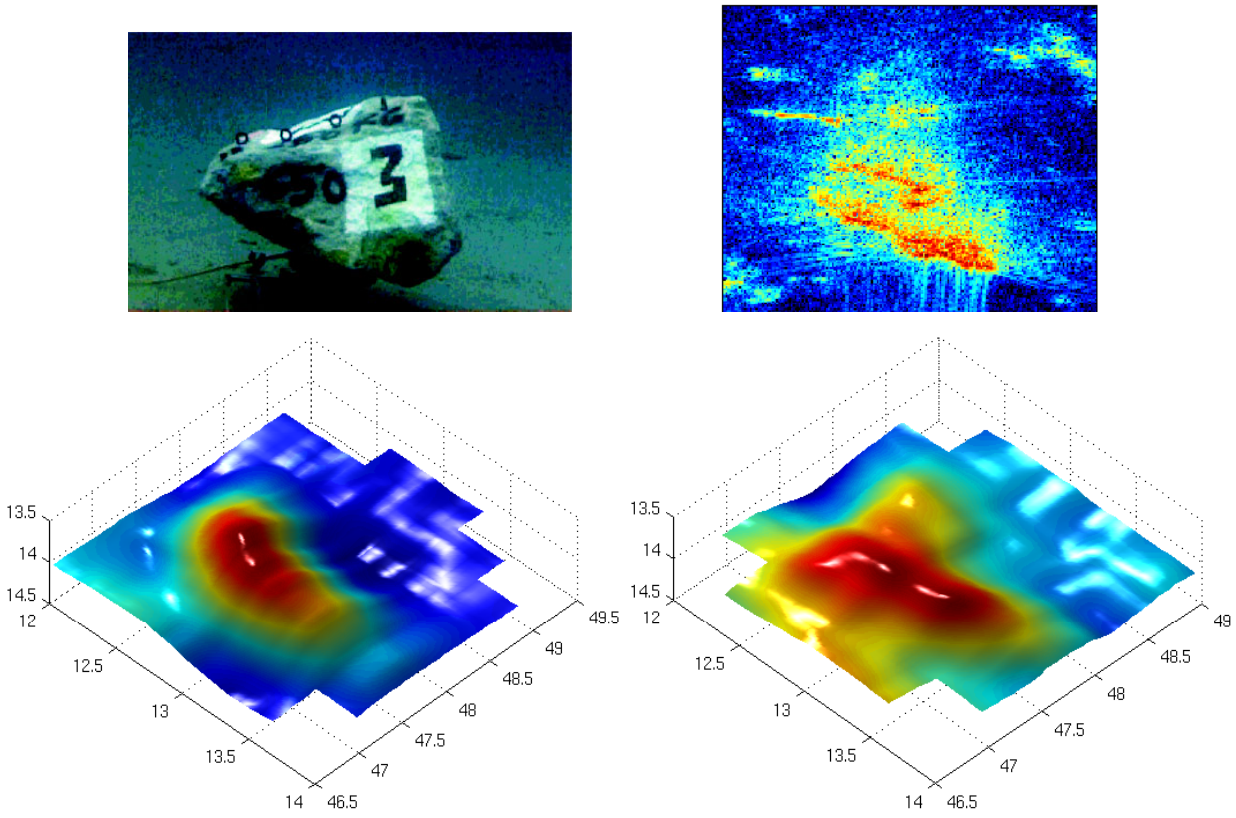

Figure 6.4 Rock on the turntable from run 221113. Upper left: Optical image. Upper right: SAS image. Lower left: coarse bathymetry. Lower right: phase unwrapped bathymetry.

7 CONCLUSION

The challenge in seafloor imaging in military applications, is to produce images of such quality that man-made objects (e.g. mines) can be separated from natural objects (rocks) of equal size with highest possible precision. To maintain high area coverage rate in cluttered environments, the sonar image resolution at far range (detection ranges) must be of “classification quality”. SAS seems to be an excellent tool for this.

A limiting factor for practical use of SAS has been the requirement for navigation accuracy. This problem is solved by fusion of sonar micronavigation with the aided INS on-board the AUV. This requires knowledge of the slant-range direction, which can only be obtained by estimating the swath bathymetry with an interferometric sensor (or prior knowledge of the seafloor). This has been solved by assuming flat seafloor for non-interferometric sensors.

Operating AUVs in areas with rough topography is optimally performed by running at constant height. This leads to out-of-plane motion deviations, which again causes defocusing without prior knowledge of the bathymetry (18). This effect is independent of choice of beamforming technique. There are techniques to compensate for this which are valid under certain assumptions (11). However, the only general solution for this problem is either running on a straight line (obtaining a focused but not correctly positioned image), or estimating the height by the use of interferometry.

Full swath cross-correlation based SAS interferometry seems feasible, and has the potential to dramatically increase the along-track resolution compared to traditional bathymetric mapping with Multi Beam Echosounders (MBE). Interferometric SAS does however have the same limitation as MBEs to height accuracy, given by the requirement of known sound velocity profile. A two-sided interferometric SAS in combination with a MBE as gap-filler seems as the natural choice for Rapid Environmental Assessment (REA) type AUV operations, where the requirement for absolute height accuracy is relaxed. High resolution mapping of objects will increase classification ability. This is, however, non-trivial, and considerable work is left before reliable 3D mapping of objects can be done.

ACKNOWLEDGMENTS

The authors would like to thank the SACLANTCEN team and the QinetiQ team involved in the InSAS-2000 trials. We especially thank Sean Chapman and his team at QinetiQ for providing and operating the high resolution Interferometric SAS system and the rail for the trials. We also thank Dr Marc Pinto and Andrea Bellettini at SACLANTCEN for many fruitful discussions.

ABBREVIATIONS

AUV	Autonomous Underwater Vehicle
AINS	Aided Inertial Navigation System
CRLB	Cramer-Rao Lower Bound
DPCA	Displaced Phase Center Antenna
FFBP	Fast Factorised Back-Projection
IMU	Inertial Measurement Unit
INS	Inertial Navigation System
INSAS	Interferometric Synthetic Aperture Sonar
MBE	MultiBeam Echosounder
PGA	Phase Gradient Algorithm
REA	Rapid Environmental Assesment
SACLANT	Supreme Allied Commander Atlantic
SACLANTCEN	SACLANT Undersea Research Centre
SAR	Synthetic Aperture Radar
SAS	Synthetic Aperture Sonar
SNR	Signal to Noise Ratio
SSS	Side Scan Sonar
TDIB	Time Domain Interpolation Beamforming

References

(1) Banks S (2002): *Studies in High Resolution Synthetic Aperture Sonar*. PhD thesis, University College London, London, UK.

(2) Bellettini A and Pinto M (2002): Theoretical Accuracy of Synthetic Aperture Sonar Micronavigation using a Displaced Phase Centre Antenna. *IEEE J. Oceanic Eng.*, 27 (4):780–789.

(3) Billon D and Fohanno F (1998): Theoretical performance and experimental results for synthetic aperture sonar self-calibration. In *Proceedings of Oceans 98*, pages 965–970, Nice, France.

(4) Billon D and Fohanno F (2002): Two improved ping-to-ping cross correlation techniques for synthetic aperture sonar: theory and sea results. In *Proceedings of Oceans 2002 MTS/IEEE*, pages 2284–2293, Biloxi, MS, USA.

(5) Bonifant Jr W W, Richards M A and McClellan J H (2001): Interferometric height estimation of the seafloor via synthetic aperture sonar in the presence of motion errors. *IEE Proc. Radar, Sonar Navig.*, 147 (6):322–330.

(6) Carrara W G, Goodman R S and Majewski R M (1995): *Spotlight Synthetic Aperture Radar: Signal Processing Algorithms*. Artech House.

(7) Chang E (2001): Synthetic Aperture Sonar - Tutorial Part II. Presented at Oceans 2001 MTS/IEEE, Honolulu, HI, USA.

(8) Cook D A, Christoff J T and Fernandez J E (2001): Broadbeam Multi-Aspect Synthetic Aperture Sonar. In *Proceedings of Oceans 2001 MTS/IEEE*, pages 188–192, Honolulu, HI, USA.

(9) Fernandez J E and Christoff J T (2000): Multi-Aspect Synthetic Aperture Sonar. In *Proceedings of Oceans 2000 MTS/IEEE*, pages 177–180, Providence, RI, USA.

(10) Franceschetti G and Lanari R (1999): *Synthetic Aperture Radar Processing*. CRC Press.

(11) Groen H, Hansen R E and Sabel J C (2003): Sonar path correction in synthetic aperture processing. In *Proceedings of UDT Europe 2003*, Malmö, Sweden.

(12) Hagen P E, Hansen R E, Gade K and Hammerstad E (2001): Interferometric Synthetic Aperture Sonar for AUV Based Mine Hunting: The SENSOTEK project. In *Proceedings of Unmanned Systems 2001*, Baltimore, MD, USA.

(13) Hagen P E, Størkersen N, Vestgård K and Kartvedt P (2003): The HUGIN 1000 Autonomous Underwater Vehicle for Military Applications. In *Proceedings of Oceans 2003 MTS/IEEE*, San Diego, CA, USA.

(14) Hansen R E (2001): SENSOTEK Interferometric Synthetic Aperture Sonar for HUGIN AUV. FFI/RAPPORT (in Norwegian) 2001/03193, Norvegian Defence Research Establishment.

(15) Hansen R E, Sæbø T O, Gade K and Chapman S (2003): Signal Processing for AUV based Interferometric Synthetic Aperture Sonar. In *Proceedings of Oceans 2003 MTS/IEEE*, San Diego, CA, USA.

(16) Hanssen A, Kongsli J, Hansen R E and Chapman S (2003): Signal Processing for AUV based Interferometric Synthetic Aperture Sonar. In *Proceedings of Oceans 2003 MTS/IEEE*, San Diego, CA, USA.

(17) Hawkins D W (1996): *Synthetic Aperture Imaging Algorithms: with application to wideband sonar*. PhD thesis, University of Canterbury, Christchurch, New Zealand.

(18) Jakowatz J C V, Wahl D E, Ghiglia D C and Thompson P A (1996): *Spotlight-Mode Synthetic Aperture Radar: A Signal Processing Approach*. Kluwer Academic Publishers.

(19) Jalving B, Gade K, Hagen O K and Vestgård K (2003): A Toolbox of Aiding Techniques for the HUGIN AUV Integrated Inertial Navigation System. In *Proceedings of Oceans 2003 MTS/IEEE*, San Diego, CA, USA.

(20) Johnson D H and Dudgeon D E (1993): *Array Signal Processing: Concepts and Techniques*. Prentice Hall.

(21) Lurton X (2000): Swath Bathymetry Using Phase Difference: Theoretical Analysis of Acoustical Measurement Precision. *IEEE J. Oceanic Eng.*, 25 (3):351–363.

(22) Medwin H and Clay C S (1998): *Fundamentals of Acoustical Oceanography*. Academic Press, Boston.

(23) Oliver C and Quegan S (1998): *Understanding Synthetic Aperture Radar Images*. Artech house, Inc.

(24) Pinto M, Hollett R D, Bellettini A and Chapman S (2001): Bathymetric imaging with wideband interferometric synthetic aperture sonar. *submitted to IEEE J. Oceanic Eng.*

(25) Pinto M A, Fioravanti S and Bovio E (1998): Accuracy of synthetic aperture sonar using a displaced phase center antenna. Saclantcen Memorandum SM-352.

(26) Pinto M A, Fioravanti S and Bovio E (1998): Multiple-Element Synthetic Aperture Sonar Design. Saclantcen note.

(27) Shippey G, Pihl J and Jönsson M (2001): Autopositioning for Synthetic Aperture Sonar using Fast Factorised Back Projection. In *Proceedings of CAD/CAC 2001*, Halifax, Canada.

(28) Soumekh M (1994): *Fourier Array Imaging*. Prentice Hall.

(29) Ulander L M H and Frölind P O (1998): Ultra-Wideband SAR Interferometry. *IEEE Trans. Geosci. Remote Sensing.*, 36 (5):1540–1550.

(30) Ulander L M H, Hellsten H and Stenström G (2001): Synthetic-Aperture Radar Processing using Fast Factorised Back-Projection. *submitted to IEEE Trans. Aerospace and Electronic Systems*.

(31) Wang L, Bellettini A, Hollett R, Tesei A, Pinto M, Chapman S and Gade K (2001): InSAS'00: Interferometric SAS and INS aided SAS imaging. In *Proceedings of Oceans 2001 MTS/IEEE*, pages 179–187, Honolulu, HI, USA.

(32) Warman K, Chick K and Chang E (2001): Synthetic Aperture Sonar Processing for Widebeam/Broadband Data. In *Proceedings of Oceans 2001 MTS/IEEE*, pages 208–211, Honolulu, HI, USA.

DISTRIBUTION LIST

FFIBM **Dato:** 26. august 2003

RAPPORT TYPE (KRYSS AV)	RAPPORT NR	REFERANSE	RAPPORTENS DATO
X RAPP ☐ NOTAT ☐ RR	2003/02740	FFIBM/808/116	26. august 2003
RAPPORTENS BESKYTTELSESGRAD		ANTALL TRYKTE UTSTEDT	ANTALL SIDER
UNCLASSIFIED		61	34
RAPPORTENS TITTEL		FORFATTER(E)	
SYNTHETIC APERTURE SONAR SIGNAL PROCESSING: RESULTS FROM INSAS-2000		HANSEN Roy Edgar, SÆBØ Torstein Olsmo	
FORDELING GODKJENT AV FORSKNINGSSJEF:		FORDELING GODKJENT AV AVDELINGSSJEF:	
Nils J Størkersen		Jan Ivar Botnan	

EKSTERN FORDELING

ANTALL	EKS NR	TIL
1		KE/MKF
1		KOM Geir Flage
1		KK Per Kartvedt
1		KL Stig Nilsen
1		FLO/Sjø
1		OK Geir Sten
1		Avding Thor Erling Jensen
1		KNM Tordenskjold
1		KL Jon Arild Strandnæs
1		KK Eirik Johannessen
1		E-tjenesten
1		Jorunn Anita Sunde
1		OK Trond Kjerre
1		FST
1		KK Rolf Magne Stein
1		FST/SST
1		Gisle Vincent Eye
		Simrad AS
1		v/ Håvard Nes
1		v/ Even Borten Lunde
		Boks 111, 3191 Horten

INTERN FORDELING

ANTALL	EKS NR	TIL
14		FFI-Bibl
1		Adm direktør/stabssjef
1		FFIE
1		FFISYS
1		FFIBM
1		FFIN
4		Forfattereksemplar(er)
6		Restopplag til Biblioteket
		Elektronisk fordeling:
		Jan Ivar Botnan (JIB)
		Nils Størkersen (NJS)
		Jarl Johnsen (JKJ)
		Tor Knudsen (TKn)
		Per Espen Hagen (PEH)
		Øivind Midtgaard (OMi)
		Bjørn Jalving (BjJ)
		Kenneth Gade (KGa)
		Svein-Erik Hamran (SEH)
		Trygve Sparr (TSp)
		Dan Weydahl (DJW)
		Knut Eldhuset (KnE)
		Åslaug Grøvlen (AGr)
		Torstein Olsmo Sæbø (TSb)
		Roy Edgar Hansen (RHn)
		FFI-veven

Benytt ny side om nødvendig

EKSTERN FORDELING

INTERN FORDELING

ANTALL	EKS NR	TIL	ANTALL	EKS NR	TIL
		Kongsberg Maritime AS			
1		v/ Rolf Arne Klepaker			
1		v/ Erik Hammerstad			
1		v/ Karstein Vestgård			
1		v/ Geir Helge Sandsmark			
1		v/ Kjersti Helene Wold			
1		v/ Ragnar Eckhoff			
1		v/ Bjørnar Langli			
		Boks 111, 3191 Horten			
1		Alfred Hanssen Institutt for Fysikk Mat-Nat Universitetet i Tromsø 9037 Tromsø			
1		Marc Pinto NATO SACLANT Undersea Research Centre V. San Bartolomeo 400, 19138 La Spezia, Italy			
1		Andrea Bellettini NATO SACLANT Undersea Research Centre V. San Bartolomeo 400, 19138 La Spezia, Italy			
1		Sean Chapman QinetiQ, Bincleaves Newton Road Weymouth Dorset DT4 8UR, UK			
1		Sverre Holm Institutt for Informatikk Universitetet i Oslo Boks 1080, 0316 Oslo			
1		Andreas Austeng Institutt for Informatikk Universitetet i Oslo Boks 1080, 0316 Oslo			